Transformations in Sol-Gel Synthesized Nanoscale Hydroxyapatite Calcined Under Different Temperatures and Time Conditions

Kapoor Seema, Batra Uma, and Kohli Suchita

Nano-hydroxyapatite (HAP) has been synthesized using sol-gel technique. Calcium nitrate tetrahydrate and potassium dihydrogen phosphate were used as precursors for calcium and phosphorus, respectively. A detailed study on its transformation during calcination at two crucial temperatures has been undertaken. The synthesized nanopowder was calcined at 600 and 800 °C for different time periods. The results revealed that the obtained powders after calcining at 600 and 800 °C are composed of hydroxyapatite nanoparticles. The nano-HAP powders were characterized by x-ray diffraction (XRD), transmission electron microscopy (TEM), Fourier transform infrared spectroscopy, thermal gravimetric analysis (TGA), and BET surface area analyzer techniques. The results indicate that crystallite size as well as crystallinity of synthesized HAP nanopowders increase with increase in calcination temperature as well as calcination time, but the effect of temperature is more prominent as compared to that of calcination time. TEM micrograph revealed the presence of majority of HAP powder particles as agglomerates and a few as individual particles. It also revealed that HAP produced after sintering at 600 °C is 26-45 nm in size, which is well in agreement with the crystallite size calculated using XRD data. TGA study showed the thermal stability of the as-synthesized nano-HAP powder. The BET surface area decreased with increase in calcination temperature and time. The results clearly demonstrate the significant role of calcination parameters on the characteristics of nano-HAP powders.

Keywords	BET surface area, biomaterials, calcination, hydroxyapatite, nanocrystalline, sol-gel

1. Introduction

Bone defects and non-unions caused by trauma, resection, or abnormal development pose a significant health problem worldwide with over 500,000 bone repair procedures performed annually (Ref 1). At present, autografts remain the gold standard for bone repair, substitution, and augmentation followed by allografts. Although autografts and allografts have important advantage of being osteogenic or osteoinductive, they suffer from some disadvantages, including high cost, trauma, and limited supply, risk of immune rejection or a chronic immune response and potential viral transmission (Ref 2). The disadvantages of autografts and allografts have prompted interest in developing the synthetic materials as bone graft substitutes.

Many commercial substitute materials have been developed, including metal, natural and synthetic polymers, corals and its derivatives, human bones (from cadaver bones), cow bones,

synthetic ceramics (calcium phosphates, calcium sulfates, calcium carbonates, bioactive glasses), and composites (Ref 3). Among these bone substitute materials, the most used materials are calcium phosphate (Ca-P)-based biomaterials (e.g., hydroxyapatite, tricalcium phosphate, octcalcium phosphate, amorphous calcium phosphate, dicalcium phosphate, etc.) (Ref 4). The reason for the development of the Ca-P-based biomaterials is their similarity in composition to the bone mineral and their good biocompatibility, bioactivity, osteoconductivity, etc.

Hydroxyapatite ($Ca_{10}(PO_4)_6(OH)_2$) is the most ubiquitous calcium phosphate that has been intensely studied over the years. One of the main reasons for the intense focus is because of its structural and compositional similarity to the mineralized matrix of natural bone. As a result, this inorganic phosphate has been studied extensively for medical applications in the form of powders, composites, or even coatings (Ref 5-9). Furthermore, it has also been studied for other non-medical applications, for example, as packing media for column chromatography, gas sensors, catalysts, etc. (Ref 5). Due to its diverse applications, the materials' properties accordingly need to be tailored for real world applications. Hence researchers have tried to customize its properties such as bioactivity, mechanical strength, solubility, and sinterability by controlling its composition, morphology, and particle size (Ref 9).

Earlier research on the development of HAP was mainly focused on controlling the stoichiometry of the products, and now with the development of nanotechnologies, a considerable interest is shown in controlling the morphology and size of HAP. Better structural biomimicity and osteoconductivity can be achieved using nanosized and nanocrystalline HAP (Ref 10-14). Biocompatibility of such biomaterials is the key factor in

Kapoor Seema and Kohli Suchita, University Institute of Chemical Engineering & Technology, Panjab University, Chandigarh 160014, India; Batra Uma, Department of Materials & Metallurgical Engineering, PEC University of Technology, Sector-12, Chandigarh 160012, India. Contact e-mails: umabatra2@yahoo.com and suchita_kohli@ yahoo.co.in.

their possible clinical use. The properties of nano-HAP prepared by various methods differ in their properties mainly due to the synthetic procedures, which in turn directly affect its bioactivity. Hence, synthesis of pure nano-HAP with controlled size and morphology is highly desirable.

Numerous HAP synthesis techniques have been developed which include mechanochemical synthesis (Ref 15), combustion preparation (Ref 16), and various techniques of wet chemistry, such as direct precipitation from aqueous solutions (Ref 17), electrochemical deposition (Ref 6), sol-gel procedures (Ref 18), hydrothermal synthesis (Ref 19), and emulsion or micro-emulsion routes (Ref 20), etc. The most commonly used technique for the preparation of HAP nanopowders is the sol-gel technique as it is an elective method for the preparation of highly pure powder due to the possibility of a strict control of the process parameters. This method offers a molecular mixing of the calcium and phosphorus, which is capable of improving the chemical homogeneity. The sol-gel product is characterized by nano-size dimension of the primary particles and this small domain is a very important parameter to improve the contact reaction and the stability at the artificial/natural bone interface.

In this study, we report the synthesis of pure, nanocrystalline HAP without any other additional phase, up to 1000 °C, giving emphasis on the effect of calcination parameters on the characteristics of nano-HAP powders using potassium dihydrogen phosphate (KH_2PO_4) as a phosphorous precursor (Ref 21). It has been noted that the effect of temperature and time of calcination on the characteristics of sol-gel synthesized nano-HAP using KH_2PO_4 as a phosphorous precursor has not been studied in detail (Ref 22).

2. Materials and Methods

2.1 Synthesis of Hydroxyapatite Nanopowders

The flowchart shown in Fig. 1 outlines the experimental procedure used to synthesize the HAP nanopowder in this study. A stoichiometric amount of calcium nitrate tetrahydrate ($Ca(NO_3)_2 \cdot 4H_2O$, Merck, AR grade), and potassium dihydrogen phosphate (Merck, AR grade) were used with the molar ratio of 10:3, which is the desired Ca/P ratio observed in hydroxyapatite (Ref 23). Deionized water was used as the solvent. 1 M solution of calcium nitrate tetrahydrate was added dropwise to 0.6 M solution of potassium dihydrogen phosphate. Mixing was done under continuous stirring conditions. The pH was adjusted to 11 by adding liquid ammonia. Increased pH of mixture is reported to significantly improve gelation process of hydroxyapatite sol-gel (Ref 23). After mixing was complete, continuous stirring was done for 1 h and the solution was aged for 24 h at room temperature. Then the solution was filtered and washed using warm double-distilled water so as to remove the undesired K^+, NH_4^+, and NO_3^{-1} ions. The gel obtained after filtration was dried at 55 °C in oven and then crushed using mortar and pestle.

The reaction involved in the formation of HAP during the sol-gel preparation and drying can be expressed as follows (Ref 23):
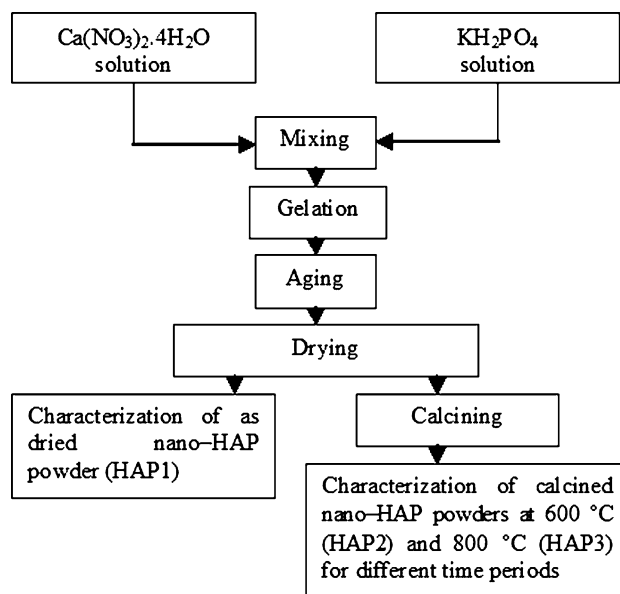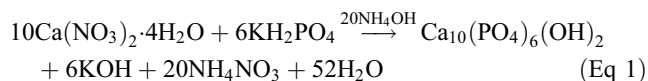
$$10Ca(NO_3)_2 \cdot 4H_2O + 6KH_2PO_4 \xrightarrow{20NH_4OH} Ca_{10}(PO_4)_6(OH)_2$$
$$+ 6KOH + 20NH_4NO_3 + 52H_2O \qquad \text{(Eq 1)}$$

Fig. 1 Flow chart of sol-gel synthesis of HAP nanopowder

The dried HAP powder was subjected to calcining at a rate of 5 °C/min up to 600 and 800 ° for different time periods in a muffle furnace and finally was placed in air for cooling to ambient temperature. The powders were labelled as: powder dried at 55 °C (HAP1), calcined at 600 °C for 1, 2, 3, and 4 h ($HAP2_1$, $HAP2_2$, $HAP2_3$, $HAP2_4$) and calcined at 800 °C for 1, 2, 3, and 4 h ($HAP3_1$, $HAP3_2$, $HAP3_3$, $HAP3_4$), respectively.

2.2 Characterization

X-ray diffraction (XRD) analysis was performed on all the nanopowders using a Philips Xpert diffractometer with CuKα ($\lambda = 1.54$ Å) radiation. The data were recorded over the 2θ range of 20° to 80° with a 0.017° step size and scan step time of 20.03 s. Phase analysis, estimation of crystallinity, and crystallite size of nanopowders were carried out from the XRD patterns obtained.

Transmission electron microscope (TEM) (Hitachi, 7500) was used to observe the particle morphology and size of the powders.

Fourier transform infrared (FTIR) spectroscopy analysis (Perkin Elmer Spectrum RXI FT-IR system) was carried out to identify the functional groups. The spectrum was recorded in the 4000-400 cm^{-1} region with 2 cm^{-1} resolution.

A Perkin Elmer STA 6000 Simultaneous Thermal Analyzer was used to study thermal gravimetric analysis (TGA) of the nano-HAP powder (HAP1). For determining the mass variation in the sample, the sample was heated from room temperature to 1000 °C, at a heating rate of 10 °C/min under nitrogen flow.

The BET surface area of the nanopowders was evaluated by N_2 adsorption (Quantachrome Instruments NOVA 2200e Surface Area Analyzer) using Brunauer-Emmett-Teller (BET) method (Ref 24). The linearized form of BET equation is expressed as:

$$\frac{p}{v(p_o - p)} = \frac{1}{v_m c} + \frac{c-1}{v_m c}\frac{p}{p_o}$$

where p/p_o is the relative vapor pressure of the adsorbate, v is the volume of gas adsorbed, v_m is the volume of gas adsorbed in a monolayer, and c is a constant related to the energy of adsorption. A linear regression of the left side of the BET equation and p/p_o yields a slope and intercept from which c and v_m are obtained. The BET surface area is then calculated from v_m (Ref 25).

3. Results and Discussion

In Fig. 2, the XRD patterns of HAP1, HAP2$_1$, and HAP3$_1$ powders are compared. All spectra show only the HAP reflections (JCPDS II 74-0566). The powders are found to be hexagonal and have matched well with JCPDS Card No. 74-0566. Both cell parameters, a and c, have been calculated using the equation given below (Ref 26):

$$\frac{1}{d^2} = 4/3 \left[\frac{h^2 + hk + l^2}{a^2} \right] + \frac{l^2}{c^2}$$

where d is the distance between adjacent planes in the set of Miller indices ($h\,k\,l$). The cell parameters of HAP1, HAP2$_1$, and HAP3$_1$ powders are reported in Table 1. On comparing the cell parameters for HAP2$_1$ and HAP1 powders, a small contraction of the reticular parameter, a, accompanies by an increase in c value resulting eventually in a slight unit cell volume decrement. The parameters a and c both have decreased for the HAP3$_1$ powder with obvious decrease in volume of unit cell. The HAP1 powder bears with it the characteristic pattern of HAP but not with much resolution and intensity. It does not contain any phase other than HAP. Broad peaks at (002) and (211) indicate that the HAP powder crystallites are tiny and poorly crystallized.

Crystallite size, X_s, is calculated using Scherrer's equation (Ref 22, 27). For this purpose, three different peaks (002), (202), and (222), which are well separated and having high intensities were chosen for the measurement. Mean crystallite size of all samples are summarized in Table 1. HAP1 has the smallest crystallite size of 20 nm. The crystallite size has increased to 42 and 67 nm for HAP2$_1$ and HAP3$_1$ powders,

respectively. The crystallinity degree (X_c) of as-dried and calcined powders, corresponding to the fraction of crystallite phase present in the examined volume was evaluated as follows (Ref 28):

$$X_c = 1 - V_{112/300}/I_{300}$$

where I_{300} is the intensity of (300) reflection of HAP and $V_{112/300}$ is the intensity of the hollow between (112) and (300) reflections, which completely disappears in noncrystalline samples. In agreement with Landi et al. (Ref 28), verification was made as follows:

$$\beta_{002} 3\sqrt{X_c} = K$$

where K is a constant equal to 0.24 for a very large number of different HAP powders, and β_{002} is the full width at half maximum (in degrees) of the (002) reflection. HAP1 powder has poor crystallinity degree of 0.12. The calcination at 600 and 800 °C has resulted into increase in crystallinity of HAP to 0.62 and 0.90, respectively. It is observed that there is significant increase in intensity and enhanced resolution of all XRD peaks when the calcination temperature is raised from 600 to 800 °C. New crystalline phases are not observed; this

Table 1 Crystallite size, crystallinity, and lattice parameters of nano-HAP powders

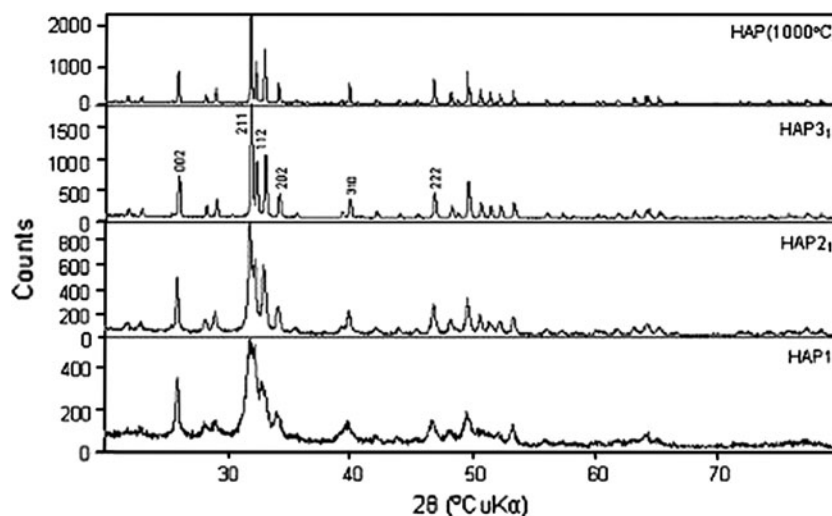| Sample	Crystallite size, nm	Crystallinity, X_c	Lattice parameters	
			$a = b$, A°	c, A°
HAP1	20.0	0.12	9.4358	6.8780
HAP2$_1$	42.0	0.62	9.4276	6.8880
HAP2$_2$	44.0	0.69	9.4251	6.8890
HAP2$_3$	45.0	0.71	9.4210	6.8900
HAP2$_4$	46.0	0.71	9.4170	6.8920
HAP3$_1$	67.0	0.90	9.4102	6.8640
HAP3$_2$	67.5	0.96	9.4085	6.8644
HAP3$_3$	68.0	0.96	9.4035	6.8687
HAP3$_4$	69.0	0.96	9.4002	6.8734

Fig. 2 XRD patterns of HAP1 (as-synthesized), HAP2$_1$ (calcined at 600 °C for 1 h) and HAP3$_1$ (calcined at 800 °C for 1 h), HAP (calcined at 1000 °C for 1 h)

precludes even amorphous phases, as the patterns appear very resolved for HAP powder calcined at 800 °C. Also increase in intensity is noticed for every peak with increase in calcination temperature from 600 to 800 °C, this implies that growth of crystal is not restricted to the planes of maximum intensity.

The XRD spectra of HAP calcined at 600 and 800 °C for four different time periods from 1 to 4 h are compared in Fig. 3(a) and (b), respectively. Variation in cell parameters a and c for the calcined HAP powder crystallites are given in Table 1. The reference for hydroxyapatite is JCPDS #74-0566 (a = 9.418 Å, c = 6.88 Å). With increase in calcination time, gradually small contraction in a parameter is accompanied by small increment in c parameter at both calcination temperatures, i.e., 600 and 800 °C, which eventually results in slight decrement in the unit cell volume. Analysis of the unit cell parameters suggests that there are minimal changes in a and c parameters after calcination of hydroxyapatite at 600 and 800 °C. The parameter a lies between 9.41 and 9.43 Å and c lies between 6.87 and 6.89 Å. These values are within the range reported in literature for stoichiometric HAP (Ref 29). The c/a ratio is approximately 0.73 for all the nanopowders, which clearly indicate the crystallographic stability of HAP nanopowders.

The crystallinity of $HAP2_2$ and $HAP2_3$ powders is 0.69 and 0.71, showing an increase in crystallinity by 11 and 3%, when the calcination time is increased from 1 to 2 h and 2 to 3 h, respectively. The increase in calcination time to 4 h has shown no further effect on crystallinity. $HAP3_1$ powder has crystallinity of 0.90, which increased by 6.6% to a value of 0.96 when calcined for 2 h and then it remained the same even after increase of calcination time to 3 or 4 h, respectively. From Table 1, it can be observed that with increase in calcination time, the crystallite size increases for either of the calcination temperatures. The morphological shape and size of nano-HAP powder ($HAP2_1$) observed using TEM is shown in Fig. 4.

The TEM image revealed the crystallite size of HAP nanopowder ($HAP2_1$) particles ranging between 26.0 and 45.6 nm, which is well in agreement with the crystallite size calculated using XRD data.

Figure 5 presents FTIR patterns for as-dried as well as calcined HAP powders. The spectra for $HAP3_1$ possess sharp and strong band at 3571 cm^{-1} corresponding to OH^{-} group and a weak broad band corresponding to strongly adsorbed and/or bound H_2O ranging between 3550 and 3350 cm^{-1} as compared to $HAP2_1$ and HAP1. The band at 1650 cm^{-1} corresponding to H_2O bending mode is more prominent in case of HAP1 as compared to $HAP2_1$ and $HAP3_1$. The strength of peak present at 1384 cm^{-1} corresponding to NO_3^{-1} group reduces in hydroxyapatite on calcination at 600 and 800 °C. There are two characteristic bands at 1093 and 1039 cm^{-1} corresponding to ν_3 mode (stretching vibration) of the
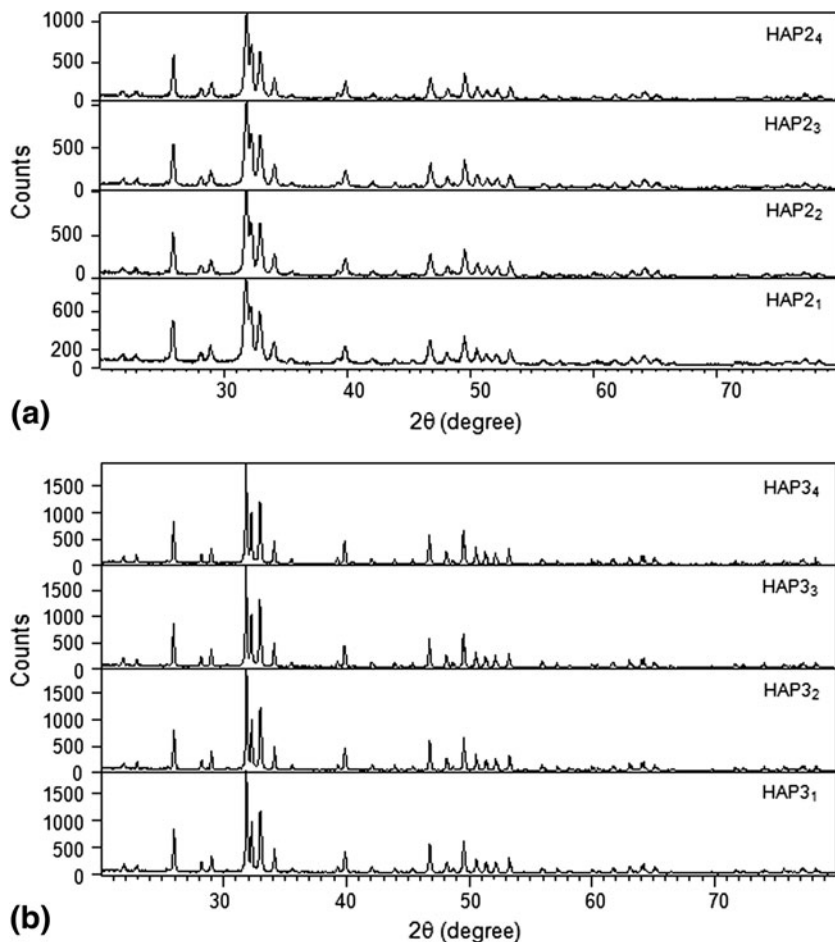

Fig. 3 (a) XRD patterns of HAP calcined at 600 °C: HAP2 (1 h), HAP2 (2 h), HAP2 (3 h), and HAP2 (4 h). (b) XRD patterns of HAP calcined at 800 °C: HAP3 (1 h), HAP3 (2 h), HAP3 (3 h), and HAP3 (4 h)
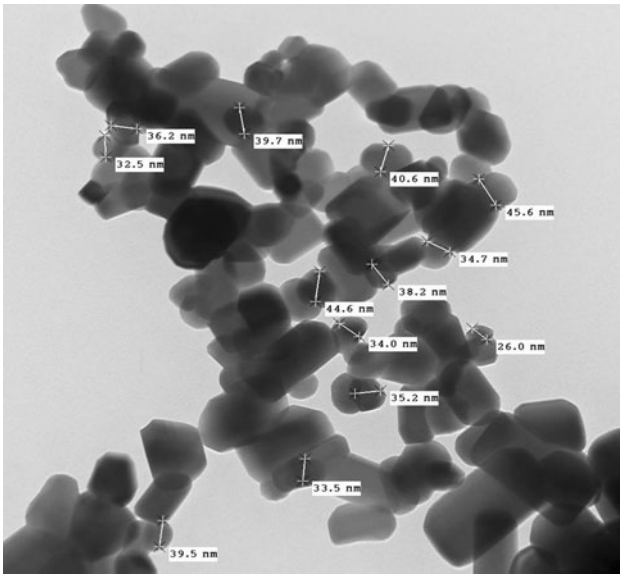
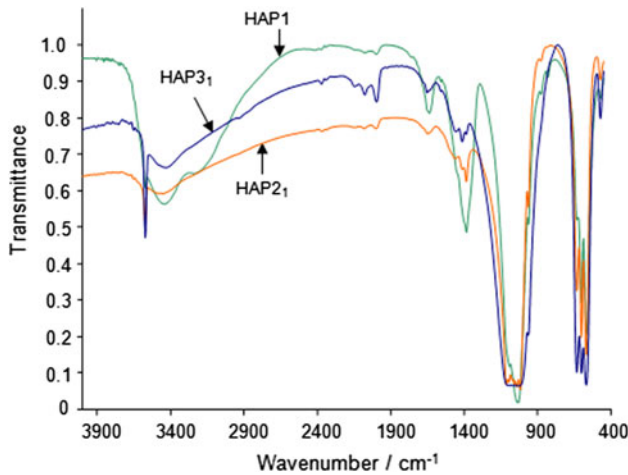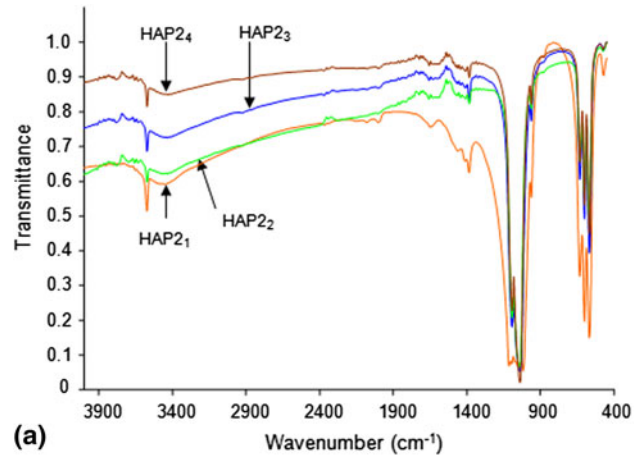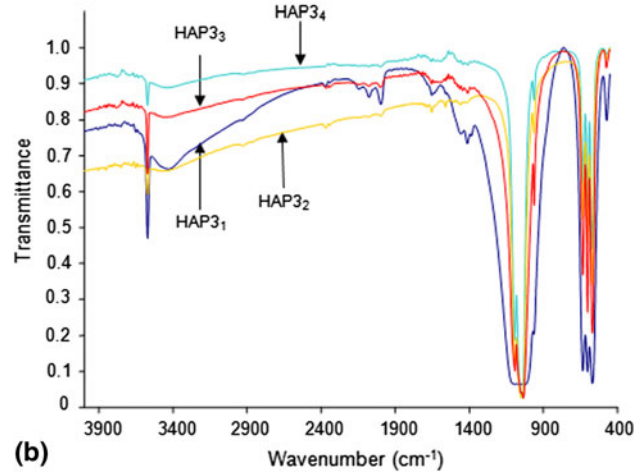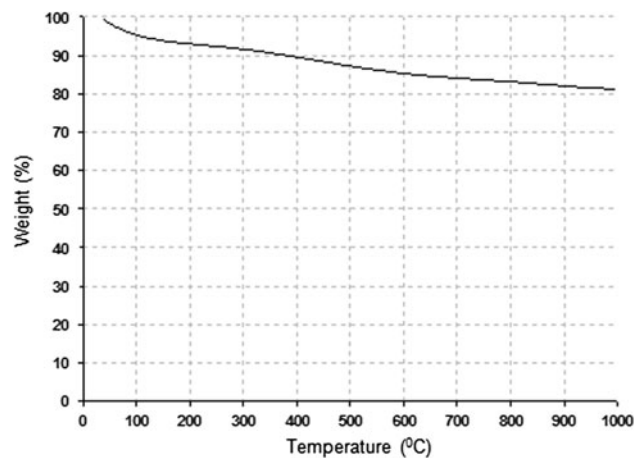**Fig. 4** TEM micrograph of HAP2 (calcined at 600 °C for 1 h)

Fig. 5 FTIR spectra of HAP1 (as-synthesized), $HAP2_1$ (calcined at 600 °C for 1 h), and $HAP3_1$ (calcined at 800 °C for 1 h)

Fig. 6 (a) FTIR spectra of HAP calcined at 600 °C: $HAP2_1$ (1 h), $HAP2_2$ (2 h), $HAP2_3$ (3 h), and $HAP2_4$ (4 h). (b) FTIR spectra of HAP calcined at 800 °C: $HAP3_1$ (1 h), $HAP3_2$ (2 h), $HAP3_3$ (3 h), and $HAP3_4$ (4 h)

Fig. 7 TGA plot of HAP1 (as-synthesized) showing the weight loss

phosphate group. The spectra show the ν_1 PO_4^{3-} mode peak at 963 cm^{-1} due to stretching vibration. The bands at 569 and 602 cm^{-1} are assigned to the ν_4 phosphate mode (bending vibration), and the peak at 473 cm^{-1} is assigned to the ν_2 phosphate mode (bending vibration). The characteristic peak at 632 cm^{-1} is due to OH$^-$ bending mode in the hydroxyapatite lattice. The bands obtained for respective phosphate and hydroxyl groups of synthesized HAP, are in agreement with other published data (Ref 23, 30, 31). FTIR patterns shown in Fig. 6(a) and (b), for HAP powders calcined at 600 and 800 °C for different time periods from 1 to 4 h, revealed that the strength of hydroxyl stretching vibration bands (at 3550-3350 cm^{-1}) has reduced substantially, while the strength of ν_3 mode PO_4^{3-} stretching vibration peaks at 1093 and 1039 cm^{-1} have increased in hydroxyapatite calcined for longer time at both the calcination temperatures.

TGA curve (Fig. 7) of the as-dried powder shows the first weight drop of 5% at temperature $T \approx 100$ °C, which is due to water evaporation. A subsequent weight loss of 13% occurs until 700 °C, which is attributed to decomposition and elimination of ammonia, nitrogenated substances as NO$_x$ and the release of gas inside the sample. However, there was very

minute weight loss on heating up to 1000 °C, which indicates the high thermal stability of the synthesized HAP. The thermal stability was also confirmed by analyzing the XRD pattern of this HAP calcined at 1000 °C, which indicated the absence of β-TCP peak (Fig. 2). Raynaud et al. (Ref 32) proved the reliability of Ca/P ratio of the initial HAP powder calculated from the proportions of HAP and β-TCP in calcined biphasic calcium phosphates. Calcium-deficient HAP changes to stoichiometric HAP and β-TCP with thermal treatment, according to the following equation:

$$Ca_{10-x}(HPO_4)_x(PO_4)_{6-x}(OH)_{2-x} \rightarrow (1-x)\ Ca_{10}(PO_4)_6(OH)_2 + 3x\beta - Ca_3(PO_4)_2 + xH_2O \qquad (Eq\ 2)$$
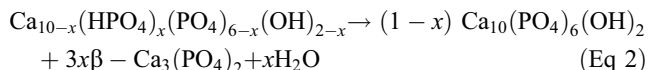
This is in agreement with the research of Yoshimura et al. (Ref 19) as well, in which he indicated that Ca-deficient HAP tends to transform to β-TCP on heating at 900 °C depending on the deficiency of calcium.

The results for BET surface area of the samples are presented in Table 2. The BET surface area of HAP1 was found to be 40.20 $m^2\ g^{-1}$ and it was observed that with an increase in temperature and/or time of calcination at 600 or 800 °C, the BET surface area decreased. The decrease in the surface area at a higher calcination temperature was due to sintering effect within the powder particles (Ref 33). In Fig. 8, the corresponding BET lines are reported for HAP1, HAP2$_1$, HAP2$_4$, HAP3$_1$, and HAP3$_4$ powders. The high correlation coefficients give evidence for the accuracy of BET surface area measurements (Ref 34).

Table 2 BET surface area of HAP1, HAP2$_1$, HAP2$_4$, HAP3$_1$, and HAP3$_4$

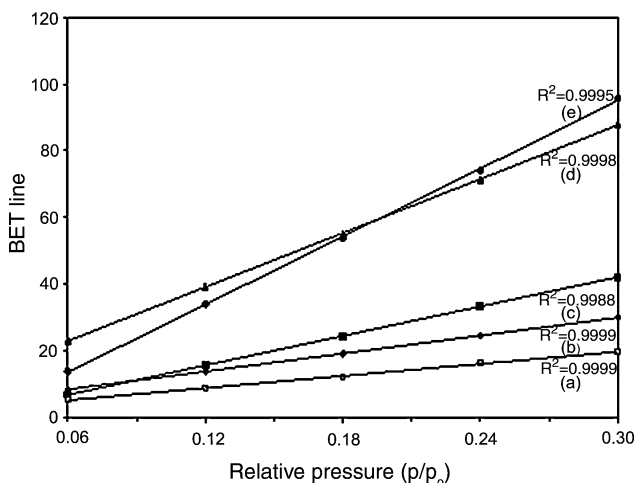| Sample	BET surface area, $m^2\ g^{-1}$
HAP	42.20
HAP2$_1$	32.40
HAP2$_4$	24.67
HAP3$_1$	11.17
HAP3$_4$	11.09

Fig. 8 BET lines for (a) HAP1; (b) HAP2$_1$; (c) HAP2$_4$; (d) HAP3$_1$; (e) HAP3$_4$

4. Conclusions

The influence of calcination temperature and time on the characteristics of nano-HAP synthesized through the water-based sol-gel process using calcium nitrate tetrahydrate and potassium dihydrogen phosphate as the precursors was investigated using XRD, electron microscopy, FTIR, thermal analysis, and BET surface area analyzer. XRD and FTIR studies confirmed the crystallized sample to be pure and nano-HAP. The crystallinity and particle size of the HAP nanopowder increased with the increase in temperature of calcination. TGA studies showed that hydroxyapatite crystals were thermally stable up to 1000 °C. The BET surface area decreased with increase in the calcination temperature and time. It is obvious that the contact reaction and the stability of the prepared nano-HAP powder at the artificial/natural bone interface can be improved by the control of its structure and surface area through calcination parameters.

References

1. R. Langer and J.P. Vacanti, Tissue Engineering, *Science*, 1993, **260**, p 920–926
2. S.W. Laurie, L.B. Kaban, J.B. Mullikan, and J.E. Murray, Donor-Site Morbidity After Harvesting Rib and Iliac Bone, *Plast. Reconstr. Surg.*, 1984, **73**, p 933–938
3. R.Z. LeGeros, Calcium Phosphate-Based Osteoinductive Materials, *Chem. Rev.*, 2008, **108**, p 4742–4753
4. M. Descamps, O. Richart, P. Hardouin, J.C. Hornez, and A. Leriche, Synthesis of Macroporous β-Tricalcium Phosphate with Controlled Porous Architectural, *Ceram. Int.*, 2008, **34**, p 1131–1137
5. K. Cheng, W. Weng, G. Han, P. Du, G. Shen, J. Yang, and J.M.F. Ferreira, The Effect of Triethanolamine on the Formation of Sol-Gel Derived Fluoroapatite/Hydroxyapatite Solid Solution, *Mater. Chem. Phys.*, 2003, **78**, p 767–771
6. L.Y. Huang, K.-W. Xu, and J. Lu, A Study of the Process and Kinetics of Electrochemical Deposition and the Hydrothermal Synthesis of Hydroxyapatite Coatings, *J. Mater. Sci. Mater. Med.*, 2000, **11**, p 667–673
7. W. Weng, G. Han, P. Du, and G. Shen, The Effect of Citric Acid Addition on the Formation of Sol-Gel Derived Hydroxyapatite, *Mater. Chem. Phys.*, 2002, **74**, p 92–97
8. W. Weng and J.L. Baptista, Alkoxide Route for Preparing Hydroxyapatite and Its Coatings, *Biomaterials*, 1998, **19**, p 125–131
9. K. Cheng, G. Han, W. Weng, H. Qu, P. Du, G. Shen, J. Yang, and J.M.F. Ferreira, Sol-gel Derived Fluorinated Hydroxyapatite Films, *Mater. Res. Bull.*, 2003, **38**, p 89–97
10. H.W. Kim, H.E. Kim, and V. Salih, Stimulation of Osteoblast Responses to Biomimetic Nanocomposites of Gelatin-Hydroxyapatite for Tissue Engineering Scaffolds, *Biomaterials*, 2005, **26**, p 5221–5230
11. M. Sato, M.A. Sambito, A. Aslani, N.M. Kalkhoran, E.B. Slamovich, and T.J. Webster, Increased Osteoblast Functions on Undoped and Yttrium-Doped Nanocrystalline Hydroxyapatite Coatings on Titanium, *Biomaterials*, 2006, **27**, p 2358–2369
12. E.S. Thian, J. Huang, S.M. Best, Z.H. Barber, R.A. Brooks, N. Rushton, and W. Bonfield, The Response of Osteoblasts to Nanocrystalline Silicon-Substituted Hydroxyapatite Thin Films, *Biomaterials*, 2006, **27**, p 2692–2698
13. Z.L. Shi, X. Huang, Y.R. Cai, R.K. Tang, and D.S. Yang, Size Effect of Hydroxyapatite Nanoparticles on Proliferation and Apoptosis of Osteoblast-Like Cells, *Acta Biomater.*, 2009, **5**, p 338–345
14. Y. Liu, G. Wang, Y. Cai, H. Ji, G. Zhou, X. Zhao, R. Tang, and M. Zhang, In Vitro Effects of Nanophase Hydroxyapatite Particles on Proliferation and Osteogenic Differentiation of Bone Marrow-Derived Mesenchymal Stem Cells, *J. Biomed. Mater. Res. A*, 2009, **90**, p 1083–1091
15. W. Kim, Q. Zhang, and F. Saito, Mechanochemical Synthesis of Hydroxyapatite from Ca(OH)$_2$-P$_2$O$_5$ and CaO-Ca(OH)$_2$-P$_2$O$_5$ Mixtures, *J. Mater. Sci.*, 2000, **35**, p 5401–5405

16. A.C. Tas, Combustion Synthesis of Calcium Phosphate Bioceramic Powders, *J. Eur. Ceram. Soc.*, 2000, **20**, p 2389–2394

17. A. Lopez-Macipe, R. Rodriguez-Clemente, A. Hidalgo-Lopez, I. Arita, M.V. Garcia-Garduno, E. Rivera, and V.M. Castano, Wet Chemical Synthesis of Hydroxyapatite Particles from Nonstoichiometric Solutions, *J. Mater. Synth. Proc.*, 1998, **6**, p 21–26

18. W. Wenjian and J.L. Baptista, Alkoxide route for preparing hydroxyapatite and its coatings. *Biomaterials* 1998, **19**, p 125–131

19. M. Yoshimura, H. Suda, K. Okamoto, and K. Loku, Hydrothermal Synthesis of Biocompatible Whiskers, *J. Mater. Sci.*, 1994, **29**, p 3399–3402

20. G.K. Lim, J. Wang, S.C. Ng, C.H. Chew, and L.M. Gan, Nanosized Hydroxyapatite Powders from Microemulsions and Emulsions Stabilized by a Biodegradable Surfactant, *J. Mater. Chem.*, 1999, **9**, p 1635–1639

21. M.H. Fathi and A. Hanifi, Evaluation and Characterization of Nanostructure Hydroxyapatite Powder Prepared by Simple Sol-Gel Method, *Mater. Lett.*, 2007, **61**, p 3978–3983

22. M.H. Fathi, A. Hanifi, and V. Mortazavi, Preparation and Bioactivity Evaluation of Bone-Like Hydroxyapatite Nanopowder, *J. Mater. Process. Technol.*, 2008, **202**, p 536–542

23. S.K. Padmanabhan, A. Balakrishnan, M.C. Chu, Y.J. Lee, T.N. Kim, and S.J. Cho, Solgel Synthesis and Characterization of Hydroxyapatite Nanorods, *Particuology*, 2009, **7**, p 466–470

24. R. Joseph and K.E. Tanner, Effect of Morphological Features and Surface Area of Hydroxyapatite on the Fatigue Behavior of Hydroxyapatite-Polyethylene Composites, *Biomacromolecules*, 2005, **6**, p 1021–1026

25. L. Clausen and I. Fabricius, BET Measurements: Outgassing of Minerals, *J. Colloid Interface Sci.*, 2000, **227**, p 7–15

26. T.J. Webster, E.A. Massa-Schlueter, J.L. Smith, and E.B. Slamovich, Osteoblast Response to Hydroxyapatite Doped with Divalent and Trivalent Cations, *Biomaterials*, 2004, **25**, p 2111–2121

27. R. Jenkins and R.L. Snyder, *Introduction to X-ray Powder Diffractometry*, Wiley, New York, 1996

28. E. Landi, A. Tampieri, G. Celotti, and S. Sprio, Densification Behaviour and Mechanisms of Synthetic Hydroxyapatite, *J. Eur. Ceram. Soc.*, 2000, **20**, p 2377–2387

29. J.C. Elliot, *Structure and Chemistry of the Apatites and Other Calcium Orthophosphates*, Elsevier, Amsterdam, 1994

30. M. Giardina and M.A. Fanovich, Synthesis of Nanocrystalline Hydroxyapatite from $Ca(OH)_2$ and H_3PO_4 Assisted by Ultrasonic Irradiation, *Ceram. Int.*, 2010, **36**, p 1961–1969

31. D. Gopi, K.M. Govindaraju, C.A.P. Victor, L. Kavitha, and N. Rajendiran, Spectroscopic Investigations of Nanohydroxyapatite Powders Synthesized by Conventional and Ultrasonic Coupled Sol-Gel Routes, *Spectrochim. Acta A*, 2008, **70**, p 1243–1245

32. S. Raynaud, E. Champion, and B. Assollant, Calcium Phosphate Apatite with Variable Ca/P Atomic Ratio II: Calcination and Sintering, *Biomaterials*, 2002, **23**, p 1073–1080

33. S. Bose and S.K. Saha, Synthesis and Characterization of Hydroxyapatite Nanopowders by Emulsion Technique, *Chem. Mater.*, 2003, **15**, p 4464–4469

34. A. Bianco, I. Cacciotti, M. Lombardi, and L. Montanaro, Si-Substituted Hydroxyapatite Nanopowders: Synthesis, Thermal Stability and Sinterability, *Mater. Res. Bull.*, 2009, **44**, p 345–354